Front. Optoelectron. 2021, 14(3): 341–351
https://doi.org/10.1007/s12200-020-1064-5

RESEARCH ARTICLE

Sb_2Se_3 film with grain size over 10 μm toward X-ray detection

Chong WANG[1*], Xinyuan DU[1*], Siyu WANG[1], Hui DENG[1,2], Chao CHEN[1], Guangda NIU (✉)[1], Jincong PANG[1], Kanghua LI[1], Shuaicheng LU[1], Xuetian LIN[1], Haisheng SONG[1], Jiang TANG (✉)[1]

1 Sargent Joint Research Center, Wuhan National Laboratory for Optoelectronics (WNLO), School of Optical and Electronic Information, Huazhong University of Science and Technology (HUST), Wuhan 430074, China
2 College of Physics and Information Engineering, Institute of Micro-Nano Devices and Solar Cells, Fuzhou University, Fuzhou 350108, China

Abstract Direct X-ray detectors are considered as competitive next-generation X-ray detectors because of their high spatial resolution, high sensitivity, and simple device configuration. However, their potential is largely limited by the imperfections of traditional materials, such as the low crystallization temperature of α-Se and the low atomic numbers of α-Si and α-Se. Here, we report the Sb_2Se_3 X-ray thin-film detector with a p–n junction structure, which exhibited a sensitivity of 106.3 μC/($Gy_{air}\cdot cm^2$) and response time of < 2.5 ms. This decent performance and the various advantages of Sb_2Se_3, such as the average atomic number of 40.8 and $\mu\tau$ product (μ is the mobility, and τ is the carrier lifetime) of 1.29×10^{-5} cm^2/V, indicate its potential for application in X-ray detection.

Keywords X-ray detector, Sb_2Se_3, p–n junction, response speed, grain size

1 Introduction

X-ray detection plays an irreplaceable role in various fields, such as medical radiography, materials characterization, and non-destructive testing of chips and constructions [1,2]. There are two main detection approaches: indirect detection and direct detection [3,4]. In the indirect system, scintillators are utilized to convert high-energy X-ray photons into low-energy visible photons that can be detected by photodetectors [5,6]. Conversely, in the direct system, X-ray photons are directly converted into electrical signals by absorber materials, which is beneficial for high sensitivity and good spatial resolution [7,8]. The commonly used amorphous Se-based direct X-ray detectors are restricted by their low atomic numbers ($Z = 34$), low carrier mobility, and short carrier lifetime [9,10]. Recently, metal halide perovskites were reported as potential direct X-ray detectors, considering the incorporation of high-Z elements (Pb, Bi, etc.) and long carrier lifetime [4,6]. However, the serious ionic migration under an electric field and the toxicity of lead still impede their practical applications [6,11,12].

Antimony selenide (Sb_2Se_3), a non-toxic and stable V–VI group semiconductor with the band gap (E_g) of ~1.1 eV, has a low melting point (~610°C) and a high vapor pressure (3.48×10^3 Pa at 600°C), which enables the convenient deposition of large-area and uniform films [13,14]. Sb ($Z = 51$) has a larger atomic number than Se ($Z = 34$), which is beneficial for the absorption of X-rays. The low band gap also results in a low generation threshold of electron–hole pairs ($W = E_g + 1.43$) [3]. Besides the advantages in the carrier generation process, the decent $\mu\tau$ product (μ is the mobility, and τ is the carrier lifetime) of Sb_2Se_3 was determined to be ~10^{-5} cm^2/V. In addition, its one-dimensional structure can suppress the crosstalk between adjacent pixels to strengthen the advantage of direct system in resolution [8]. All these features portend Sb_2Se_3 as an alternative absorber material for application in X-ray detectors.

Hence, in this study, we fabricated a Sb_2Se_3 thin-film X-ray detector. The Sb_2Se_3 film was deposited by the close-spaced sublimation (CSS) method, resulting in a high-quality film with a large grain size of > 10 μm. Further, the Sb_2Se_3/TiO_2 p–n junction structure was introduced into the device to efficiently suppress the dark current and achieve a high sensitivity of 106.3 μC/($Gy_{air}\cdot cm^2$) under an applied bias of -1 V. Because of the decent $\mu\tau$ product and thin absorber layer, in addition to the built-in electric field in the p–n junction, our Sb_2Se_3 device showed a 3 dB cutoff frequency of > 400 Hz, which is higher than the normal requirement of 30 Hz in dynamic digital radiography

Received July 1, 2020; accepted October 29, 2020

E-mails: guangda_niu@mail.hust.edu.cn (G. Niu), jtang@mail.hust.edu.cn (J. Tang)

*These authors contributed equally to this work.

[15,16]. We believe that our work would pave the way for the potential applications of Sb_2Se_3 in X-ray detection.

2 Experimental details

2.1 Device fabrication

The TiO_2 film was deposited on a cleaned fluorine-doped tin oxide (FTO) conductive glass by the spray pyrolysis method following procedures in Refs. [17,18]. The annealing temperature was set to 550°C. Subsequently, the Sb_2Se_3 layer was deposited in a homemade CSS system, modified from a rapid thermal processing instrument (OTF-1200, Hefei Kejing Materials Technology Co., Ltd.). A cleaned white glass (5 cm × 5 cm) uniformly covered with 0.4 g of Sb_2Se_3 powder (99.999%, Jiangxi Ketai Advanced Materials Co., Ltd.) was placed on an aluminum nitride ceramic plate as the source. The FTO/TiO_2 was face-down mounted above the powder as the substrate and was covered by a graphite block (10 cm × 6 cm × 1 cm) to maintain the temperature. The whole deposition process was conducted under a vacuum of ~5 × 10^{-3} Torr. First, the temperature of the substrate was increased to 400°C in 60 s and maintained for 15 min to ensure a stable high substrate temperature. Thereafter, the temperature of the source was increased to 600°C in 60 s, and the evaporation only continued for 30 s. Finally, the sample was taken out after cooling to room temperature and was subsequently thermally evaporated with an Au electrode (area: 0.09 cm^2).

2.2 Growth of Sb_2Se_3 single crystal

The melt growth of the Sb_2Se_3 single crystal was based on a reported method [19]. The internal diameter of our ampoule was 8 mm, and the furnace was a two-zone vertical Bridgman furnace (OTF-1200X-S-VT-BMGH, Hefei Kejing Materials Technology Co., Ltd.). The peak temperature was set to 624.7°C to guarantee the sufficient melting of Sb_2Se_3. The temperature gradient was ~5 °C/cm, and the ampoule moving speed was 117 nm/s. After approximately 7 days, we obtained a Sb_2Se_3 single crystal in the ampoule. The crystal was cut into ~1-mm-thick slices and subsequently evaporated with an Au electrode on both sides after polishing with a 7000-M sandpaper. The thickness of the crystal slice used in the test was measured as 900 μm, and the Au electrode area was 0.04 cm^2. All the photos are shown in Fig. S1.

2.3 Measurement and characterization

X-ray diffraction (XRD) patterns were measured using an X-ray diffractometer with Cu–Kα radiation (Empyrean, PANalytical B.V.). The surface morphology and cross section of the devices were analyzed by scanning electron microscopy (SEM, FEI Nova NanoSEM450). We used an Au anode X-ray tube (Newton Scientific M237) as the source with a maximum output of 10 W and a X-ray focal spot size of 5 μm. The X-ray source was operated with a constant acceleration voltage of 50 kV. The dose rate was modulated by changing the X-ray tube current and was calibrated with a Radcal ion chamber (model: 10 × 6–180) dosimeter. An electrometer (Keithley 2635 Source Meter) was employed to measure the current–voltage (I–V) curve and the X-ray response current. For the 3 dB cutoff frequency ($f_{3\ dB}$) measurement, a bias of -4 V was applied to the device using a low-noise current amplifier (SR570), and the output was connected to the oscilloscope (Keysight DSOS054A). SR570 worked in the high bandwidth mode without requiring any filter. For the X-ray response, an optical chopper with lead plates was used to cut off the X-ray source and provide periodic X-ray exposure. To measure the $\mu\tau$ product, a 532-nm laser was used, and the response was measured by an Agilent B1500A analyzer. All measurements were carried out at room temperature.

3 Results and discussion

The performance of a direct X-ray detector is mainly determined by two processes: X-ray absorption and carrier transportation. X-ray photons have considerably higher energy than visible light photons (more than 10000 times higher); consequently, they mainly interact with inner-shell electrons, whereas the visible photons interact with valance electrons [2,4]. Thus, the X-ray absorption coefficient (α) is highly related to the number of inner electrons and can be approximately defined by the formula, $\alpha \propto \rho Z^4/E^3$ (where ρ is the mass density, Z is the average atomic number, and E is the energy of X-ray photons) [3]. For Sb_2Se_3, the average atomic number is 40.8, and the density is 5.84 g/cm^3, which are both larger than those of α-Si (Z = 14, ρ = 2.28 g/cm^3) [20,21] and α-Se (Z = 34, ρ = 4.26 g/cm^3) [22–24], two main commercial flat-panel X-ray detector materials. The absorption coefficients of these three materials in the radiation energy range of 0.01–100 MeV (Fig. 1(a)) were calculated according to the photon cross section database [25]. Apart from the small region around 0.02 MeV, which is attributed to the resonant absorption at the K-edge of Se atoms, the absorption coefficient of Sb_2Se_3 is higher than that of the other two materials across the range. Figure 1(b) shows the attenuation ratio of these three materials with different film thickness under 30 keV X-ray photons, which is the peak of our X-ray source spectrum. Undoubtedly, Sb_2Se_3 films of the same thickness can absorb more X-ray irradiation, because the corresponding absorption coefficient of Sb_2Se_3 is the highest among the three materials.

For the carrier transport process, the $\mu\tau$ product is the key parameter that directly affects the collection of photo-generated carriers. To obtain this parameter, we produced an Sb_2Se_3 single crystal, which is preferred for $\mu\tau$ product measurement [26,27], and cut it into 900-μm-thick slices. Thereafter, we derived the $\mu\tau$ product, employing the following modified Hecht equation to fit the photoconductivity, which is widely used in single-crystalline radiation detectors [8,28]:

$$I = \frac{I_0 \mu\tau V}{d^2} \frac{1 - \exp\left(-\frac{d^2}{\mu\tau V}\right)}{1 + \frac{d}{V}\frac{s}{\mu}}, \tag{1}$$

where I_0 is the saturated photocurrent, V is the bias voltage, and d is the thickness. As shown in Fig. 1(c), the $\mu\tau$ product value of Sb_2Se_3 is calculated as 1.29×10^{-5} cm^2/V.

Beyond that, the Sb_2Se_3 film is composed of one-dimensional $(Sb_4Se_6)_n$ chains [29]. In this structure, it has strong covalent bonds along the [001] axis, whereas only weak Van der Waals interactions are present in the [100] and [010] axes. Thus, the carrier mobility along [001] has been reported to be 2–4 times larger than that along the [100] or [010] axes [30], which leads to the anisotropic current ratio of ~2.5 measured on an Sb_2Se_3 nanosheet [31]. When the film is [*hk*1]-oriented (inclined to the substrate) or even [001]-oriented (vertical to the substrate), the crosstalk between adjacent pixels can be effectively reduced, leading to a high spatial resolution.

To build a prototype X-ray detector, we subsequently attempted to deposit a Sb_2Se_3 film because it is easier to fabricate a large-area flat-panel detector than a single crystal. For one, the grain of the Sb_2Se_3 film is expected to be adequately large so that its quality is similar to that of the single crystal. For another, the Sb_2Se_3 film should have a [*hk*1]-dominant orientation to improve the carrier transportation efficiency and reduce crosstalk. However, the deposition of this optimal Sb_2Se_3 film is significantly challenging. The one-dimensional structure facilitates growth along the chains, as the Sb–Se bond energy along the chains is considerably larger than the Van der Waals force between the chains [32]. Thus, when the film has a [*hk*1]-dominant orientation, it usually shows rod-like or sheet-like grains rather than compact large grains [33,34]. These rod-like or sheet-like films have roughness of hundreds of nanometers and are unsuitable for application in detectors. As far as we know, the largest grain size of smooth and compact Sb_2Se_3 films ever reported is ~1–2 μm [32,35–37].

To overcome this challenge, the CSS method (Fig. 2(a)) was chosen, because the unique structural design of the CSS equipment can promote a high deposition rate, which is essential for increasing the size of [*hk*1]-oriented grains [32]. First, the equipment has two independent pairs of heaters and thermal couples for controlling the temperatures of the substrate and source, respectively. Therefore, we can achieve a large temperature difference between the source and substrate, which would result in a high deposition rate. Second, the short distance between the source and substrate can effectively prevent the diffusion of Sb_2Se_3 vapor and further improve the deposition rate. In addition, the nucleation site density has been proven to significantly influence the Sb_2Se_3 grain size [38]. Thus, we chose the TiO_2 film as the substrate, on which Phillips et al. obtained a Sb_2Se_3 film with a 2-μm grain size by the CSS method [35]. Our device structure was designed as illustrated in Fig. 2(b). To further enlarge the grain, we increased the annealing temperature of the TiO_2 layer from 450°C to 550°C. The layer annealed at 550°C was more inert and was newly reported to support the fabrication of Sb_2S_3 films with a large grain size of 10 μm [18], which has a similar one-dimensional structure with that of Sb_2Se_3. The results also revealed that the TiO_2 layer annealed at 550°C had a higher crystallinity and smoother surface than that at 450°C (Fig. S2).

During the film deposition process, the substrate temperature was set to 400°C to further decrease the

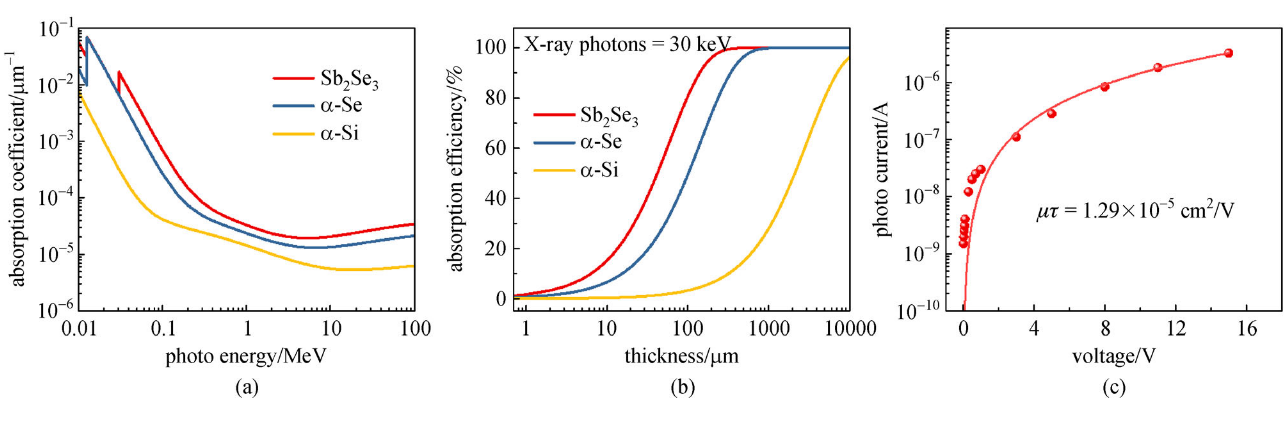

Fig. 1 (a) Absorption coefficients of Sb_2Se_3, α-Se, and α-Si at an X-ray photon energy range of 0.01–100 MeV. (b) Absorption efficiencies of Sb_2Se_3, α-Se, and α-Si toward 30 keV X-ray photons, as a function of the film thickness. (c) Bias-dependent photocurrent of the Sb_2Se_3 single crystal slice under 532-nm laser light

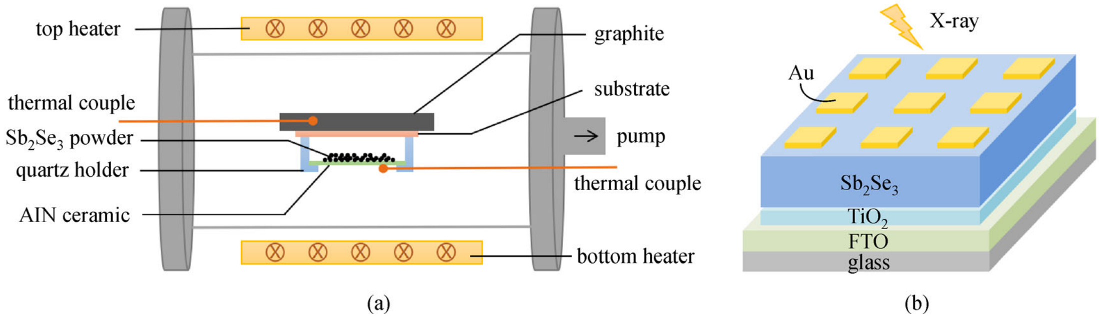

Fig. 2 (a) Schematic illustration of the homemade close-spaced sublimation (CSS) system. (b) Device architecture of the Sb_2Se_3 heterojunction thin-film X-ray detector

nuclei density. This high substrate temperature can also supply enough energy to promote the bonding process between the substrate and the Sb_2Se_3 chains, which can enhance the formation of [*hk*1]-oriented nuclei. Subsequently, by setting the source temperature to 600°C to ensure a sufficient deposition rate, we successfully obtained the Sb_2Se_3 film with a grain size of 10–20 µm. As shown in Fig. 3(a), the grains are compact and without pinholes. Further, they are more than ten times larger than the normal Sb_2Se_3 grains. From the cross-sectional SEM image (Fig. 3(b)), it can be observed that the thickness of the film reaches 5–6 µm. There is no discernible grain boundary within the large grains, which indicates that they are not composed of small grains but indeed single large grains. In addition, the corresponding XRD pattern (Fig. 3(c)) supports that the (*hk*1) peaks are dominant. The three strongest peaks are in order of (141), (061), and (041), which agrees well with the reported common orientation of Sb_2Se_3 films deposited at high substrate temperatures [32].

As a reference, under the same condition, we fabricated a Sb_2Se_3 film on a TiO_2 layer annealed at 450°C. The film exhibited a sheet-like morphology (Fig. S3) due to the relatively high nuclei density, attributed to the high number of nucleation sites. A similar sheet-like morphology was also obtained when the substrate temperature was decreased to 380°C (Fig. S4), which is also due to the relatively high nuclei density. Conversely, when we slightly changed the source temperature, the film morphology changed significantly. The film deposited at 590°C has

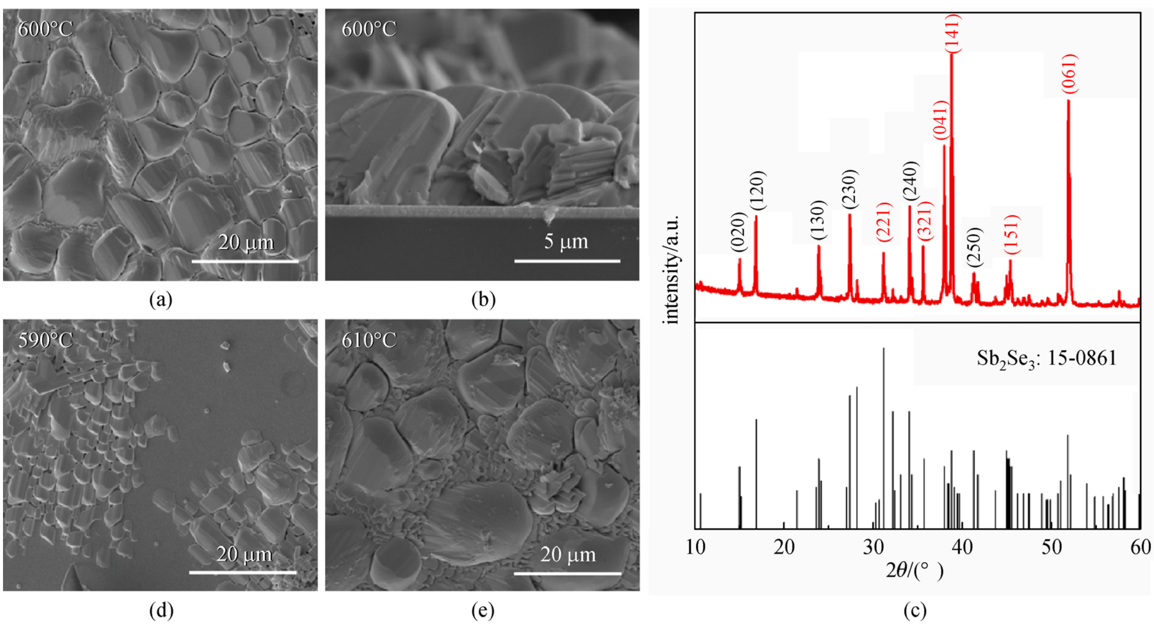

Fig. 3 Film deposition and characterization. (a) Top-down and (b) cross-sectional scanning electron microscopy (SEM) images of the large grain Sb_2Se_3 film on the TiO_2/FTO substrate (substrate temperature: 400°C, source temperature: 600°C). (c) X-ray diffraction (XRD) pattern of the large grain Sb_2Se_3 film and the corresponding Sb_2Se_3 standard powder diffraction pattern (JCPDS 15-0861). The (*hk*1) planes inclined to the substrate are signaled in red, whereas the black labels show the parallel (*hk*0) planes. Top-down SEM images of the Sb_2Se_3 film with source temperatures of (d) 590°C and (e) 610°C (substrate temperature: 400°C)

noticeably small grains and is discontinuous (Fig. 3(d)). The low source temperature cannot supply sufficient Sb_2Se_3 vapor to complete the re-evaporation of the Sb_2Se_3 film at a high substrate temperature. On the contrary, as Fig. 3(e) shows, the relatively high source temperature (610°C) results in large grains co-existing with many small grains, because the excessive supply of Sb_2Se_3 vapor facilitates the formation of new nuclei. These results highlight the requirements for obtaining an ideal Sb_2Se_3 film for X-ray detection: (a) an inert substrate, (b) a high substrate temperature, and (c) an appropriate source temperature.

On the basis of the optimized Sb_2Se_3 film, we built a direct X-ray detector and measured its performance. As the *I–V* curve shows (see Fig. 4(a)), the dark current density is over 10 mA/cm^2 under a positive bias, whereas under a negative bias, the current density significantly drops to ~10^{-3} mA/cm^2. The high rectification ratio of ~10000 indicates the good p–n junction quality of our device. The current in the negative bias range is almost a horizontal line, which suggests that there is almost no leaking channel in our device. This provides a stable working state for X-ray detection. As shown in Fig. 4(b), the dark current was ~91.2 nA when the device was operating under −1 V bias. After the X-ray was turned on with a dose rate of 5.499 mGy$_{air}$/s, the device obtained a photocurrent of ~143.8 nA. The corresponding sensitivity was calculated to be 106.3 μC/(Gy$_{air}$·cm^2), which is more than five times that of α-Se X-ray detectors (22 μC/(Gy$_{air}$·cm^2)) [39]. The stability and radiation hardness of our device were also tested (Fig. S6). After storing in air for more than half a year or exposing to nearly 900 Gy$_{air}$ X-ray radiation, the dark current and sensitivity of our devices exhibited almost no change.

By adjusting the operating current of the X-ray tube, the response for different X-ray dose rates was also investigated under the same −1 V bias. The results are shown in Fig. 4(c), which suggest that our device has significant linearity in the X-ray dose rate range of 0.5–5.5 mGy$_{air}$/s. Furthermore, we tested the sensitivity of the device under different biases ranging from 0 to −10 V. As shown in Fig. 4(d), with the enhancement of the bias, the sensitivity of our device gradually increased and finally reached ~240 μC/(Gy$_{air}$·cm^2) under −9 V bias, which is 12 times that of α-Se detectors.

Compared with photoconductive detectors, our detector has an internal depletion region, in which carriers are depleted under the built-in electric field. When X-ray irradiation occurs, the electron–hole pairs generated therein are quickly separated and drifted by the built-in

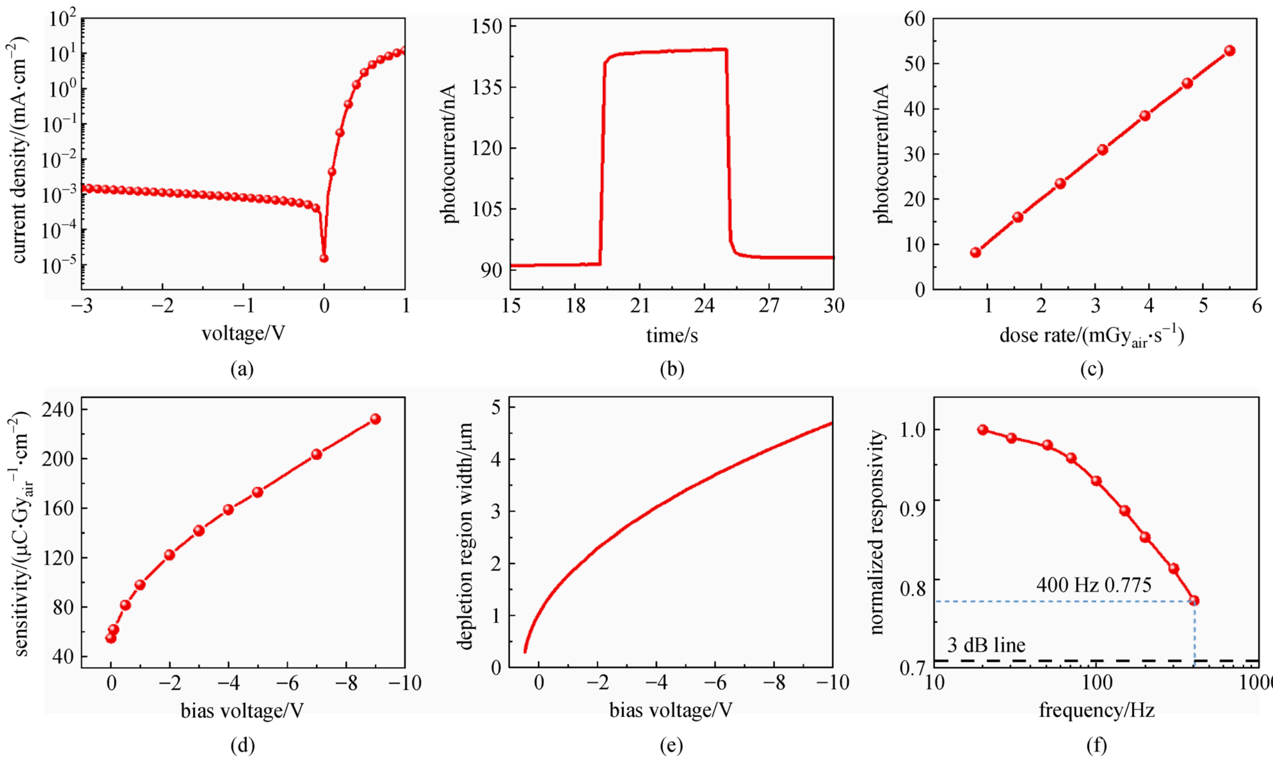

Fig. 4 X-ray detection performance. (a) Current–voltage (*I–V*) curve of devices with the structure of Au/Sb_2Se_3/TiO_2/FTO/glass. The anode was connected to the Au side. (b) Device response to X-rays (dose rate: 5.499 μGy$_{air}$/s) under a bias of −1 V. (c) Photocurrent of the detector under different dose rates (bias: −1 V). (d) X-ray sensitivity of the detector under different biases (dose rate: 5.499 μGy$_{air}$/s). (e) Calculated depletion region width in the Sb_2Se_3/TiO_2 junction versus the bias voltage. (f) Normalized responsivity of the device varies with the input X-ray frequency (bias: −4 V)

electric field. Thus, the carrier recombination can be remarkably decreased, which implies that more photo-generated carriers can be collected by the electrodes. In addition, under the reverse bias, the built-in electric field is further strengthened, and the width of the depletion region expands. Therefore, the stronger the applied reverse bias, the higher the carrier collection efficiency and detection sensitivity of our devices.

To demonstrate the effect of the depletion region, we calculated the depletion region width (X_D) of the device under different biases (V). A common model of an abrupt junction was assumed, in which TiO_2 was considered as heavily doped; thus, the depletion region was all in the Sb_2Se_3 side. The equation is as follows [40]:

$$X_D \approx \chi_p = \sqrt{\frac{2\varepsilon_r\varepsilon_0(V_D - V)}{qN_A}}, \tag{2}$$

where χ_p is the depletion region width in the p-type side; ε_0 is the vacuum permittivity, which equals 8.85×10^{-14} F/cm; ε_r is the relative permittivity of the p-type material, and here, we use 19 for Sb_2Se_3 [30]; V_D is the contact electric potential difference, and here, we use the reported middle value (0.5 V) for Sb_2Se_3 [41,42]; q is the charge of one electron, which equals 1.6×10^{-14} C; N_A is the acceptor dopant concentration of the p-type material, and here, we use 10^{13} cm^{-3} for Sb_2Se_3 [30]. As Fig. 4(e) shows, with an increase in the applied bias, the depletion region width, and device sensitivity exhibit similar trends, which fully illustrate the importance of the designed p–n junction structure for sensitivity enhancement.

In addition, the p–n junction structure has a significant effect on the response speed of our device. As mentioned above, after applying the reverse bias, the depletion region widens, but the total transportation distance of the photo-generated carriers remains fixed. Thus, the proportion of drift motion under the built-in electric field increases. This can shorten the carrier transit time, because the carrier drift speed in the depletion region is much higher than the diffusion speed in the neutral region. More importantly, because of the high drift speed provided by the built-in electric field, carriers have a low probability to be caught in traps. Thus, the relaxation time of both the rising and falling edges in the response curve can be greatly reduced, resulting in an increased response speed, even with the same trap concentration. We attempted to measure the response speed of our device by varying the frequency of the X-ray signal, which was controlled using a modified chopper with lead chips. However, because of the speed limit of our chopper, the highest X-ray frequency we could achieve was 400 Hz. As shown in Fig. 4(f), at this frequency, the normalized responsivity of our device was 0.775, which is still higher than the 3 dB line (~0.707). Therefore, we conclude that the 3 dB cutoff frequency of our device is higher than 400 Hz, and the corresponding response time is < 2.5 ms.

To identify the potential application field of our Sb_2Se_3 X-ray detector, we compared the parameters of several film-based direct X-ray detectors (Table 1). Although some newly developed perovskite and traditional CdZnTe X-ray detectors have a higher sensitivity than our device due to their high atomic number, our device has a thinner active layer. Thin-film X-ray detectors have been attracting increasing attention [45,52], and researchers are aiming to achieve flexibility, large-area, light weight, low bias, and low cost [47,50]. These detectors demonstrate unique superiority in various applications, such as the detection of cracked oil pipelines, dental radiography, portable security devices, and space exploration missions [51–54]. In this niche application, common materials such as α-Se, organic materials, and metal oxide materials all have lower average atomic numbers than Sb_2Se_3 and result in relatively low

Table 1 Comparison of several film-based direct X-ray detectors

material	thickness/μm	voltage/V	X-ray energy/keV	sensitivity/(μC·Gy_{air}^{-1}·cm^{-2})	response speed/ms	Ref.
$CsPbBr_3$	240	1.2	50	55684	92	[43]
$MAPbI_3$	830	200	100	11000	~10	[1]
CdZnTe	300	120	80	1440	NA	[44]
α-Se	200	2000	60	22	NA	[39]
TIPS-pentacene$^{1)}$	0.1	0.2	35	0.77	NA	[45]
TIPS-pentacene:PS	transistor structure		35	1300	NA	[46]
α-Ga_2O_3	0.25	50	40	6.8	NA	[47]
$MAPbI_3$	0.6	0	75	1.5	NA	[48]
$(BA)_2(MA)_2Pb_3I_{10}$	0.47	0.5	10.91	13	NA	[49]
triple cation perovskite$^{2)}$	0.45	0.4	35	97	NA	[50]
triple cation perovskite$^{3)}$	3.7	0.1	70	59.9	NA	[51]
Sb_2Se_3	5	−1	50	106.3	< 2.5	this work

Notes: 1) bis (triisopropylsilylethynyl) pentacene; 2) $Cs_{0.05}FA_{0.79}MA_{0.16}Pb\ (I_{0.8}Br_{0.2})_3$; 3) $Cs_{0.05}FA_{0.79}MA_{0.16}Pb\ (I_{0.8}Br_{0.2})_3$

sensitivities. Moreover, compared with the perovskite-based thin-film X-ray detectors, our Sb_2Se_3 device has no ionic migration; thus, a relatively high bias can be applied, resulting in a high sensitivity.

4 Conclusions

The X-ray detector application of Sb_2Se_3 was explored, due to its strengths over commercialized α-Se and α-Si, such as its larger atomic number, higher mass density, and lower generation threshold of electron–hole pairs. The inert TiO_2 substrate and high substrate temperature to reduce nucleation density, along with a high source temperature to regulate orientation and morphology, were applied together to modify the CSS process and produce an Sb_2Se_3 film with a grain size of 10–20 μm. This successful experience can be expanded to other low-dimension materials, since the same challenge may be faced in the deposition of large grain films. Meanwhile, the introduction of the p–n junction structure efficiently reduced the dark current and enhanced the device performance. Finally, our Sb_2Se_3 thin-film X-ray detector exhibited a sensitivity of 106.3 $\mu C/(Gy_{air} \cdot cm^2)$ and a response frequency of >400 Hz. These adequate performances and the unique one-dimensional structure of Sb_2Se_3 demonstrated its significant application potential in X-ray detection.

Acknowledgements This work was supported by the National Natural Science Foundation of China (Grant Nos. 61725401 and 61904058), the National Key R&D Program of China (No. 2016YFA0204000), the Innovation Fund of Wuhan National Laboratory for Optoelectronics (WNLO), the National Postdoctoral Program for Innovative Talent (No. BX20190127), and China Postdoctoral Science Foundation Project (No. 2019M662623). The authors thank the Analytical and Testing Center of Huazhong University of Science and Technology (HUST) and the facility support of the Center for Nanoscale Characterization and Devices, WNLO-HUST.

References

1. Kim Y C, Kim K H, Son D Y, Jeong D N, Seo J Y, Choi Y S, Han I T, Lee S Y, Park N G. Printable organometallic perovskite enables large-area, low-dose X-ray imaging. Nature, 2017, 550(7674): 87–91
2. Chen Q, Wu J, Ou X, Huang B, Almutlaq J, Zhumekenov A A, Guan X, Han S, Liang L, Yi Z, Li J, Xie X, Wang Y, Li Y, Fan D, Teh D B L, All A H, Mohammed O F, Bakr O M, Wu T, Bettinelli M, Yang H, Huang W, Liu X. All-inorganic perovskite nanocrystal scintillators. Nature, 2018, 561(7721): 88–93
3. Pan W, Wu H, Luo J, Deng Z, Ge C, Chen C, Jiang X, Yin W J, Niu G, Zhu L, Yin L, Zhou Y, Xie Q, Ke X, Sui M, Tang J. $Cs_2AgBiBr_6$ single-crystal X-ray detectors with a low detection limit. Nature Photonics, 2017, 11(11): 726–732
4. Wei H, Huang J. Halide lead perovskites for ionizing radiation detection. Nature Communications, 2019, 10(1): 1066
5. Yang B, Yin L, Niu G, Yuan J H, Xue K H, Tan Z, Miao X S, Niu M, Du X, Song H, Lifshitz E, Tang J. Lead-free halide Rb_2CuBr_3 as sensitive X-ray scintillator. Advanced Materials, 2019, 31(44): 1904711
6. Gao L, Yan Q F. Recent advances in lead halide perovskites for radiation detectors. Solar RRL, 2020, 4(2): 1900210
7. Wei W, Zhang Y, Xu Q, Wei H T, Fang Y J, Wang Q, Deng Y H, Li T, Gruverman A, Cao L, Huang J S. Monolithic integration of hybrid perovskite single crystals with heterogenous substrate for highly sensitive X-ray imaging. Nature Photonics, 2017, 11(5): 315–321
8. Zhuang R Z, Wang X J, Ma W B, Wu Y H, Chen X, Tang L H, Zhu H M, Liu J Y, Wu L L, Zhou W, Liu X, Yang Y. Highly sensitive X-ray detector made of layered perovskite-like $(NH_4)_3Bi_2I_9$ single crystal with anisotropic response. Nature Photonics, 2019, 13(9): 602–608
9. Huang H Y, Abbaszadeh S. Recent developments of amorphous selenium-based X-ray detectors: a review. IEEE Sensors Journal, 2020, 20(4): 1694–1704
10. Zhu M, Niu G, Tang J. Elemental Se: fundamentals and its optoelectronic applications. Journal of Materials Chemistry C, Materials for Optical and Electronic Devices, 2019, 7(8): 2199–2206
11. Jeong D N, Yang J M, Park N G. Roadmap on halide perovskite and related devices. Nanotechnology, 2020, 31(15): 152001
12. Cheng X, Yang S, Cao B Q, Tao X T, Chen Z L. Single crystal perovskite solar cells: development and perspectives. Advanced Functional Materials, 2020, 30(4): 1905021
13. Zeng K, Xue D J, Tang J. Antimony selenide thin-film solar cells. Semiconductor Science and Technology, 2016, 31(6): 063001
14. Xue D J, Shi H J, Tang J. Recent progress in material study and photovoltaic device of Sb_2Se_3. Acta Physica Sinica, 2015, 64(3): 038406 (in Chinese)
15. Yaffe M J, Rowlands J A. X-ray detectors for digital radiography. Physics in Medicine and Biology, 1997, 42(1): 1–39
16. Kim H K, Cunningham I A, Yin Z, Cho G. On the development of digital radiography detectors: a review. International Journal of Precision Engineering and Manufacturing, 2008, 9(4): 86–100
17. Chen C, Zhao Y, Lu S, Li K, Li Y, Yang B, Chen W, Wang L, Li D, Deng H, Yi F, Tang J. Accelerated optimization of TiO_2/Sb_2Se_3 thin film solar cells by high-throughput combinatorial approach. Advanced Energy Materials, 2017, 7(20): 1700866
18. Deng H, Zeng Y, Ishaq M, Yuan S, Zhang H, Yang X, Hou M, Farooq U, Huang J, Sun K, Webster R, Wu H, Chen Z, Yi F, Song H, Hao X, Tang J. Quasiepitaxy strategy for efficient full-inorganic Sb_2S_3 solar cells. Advanced Functional Materials, 2019, 29(31): 1901720
19. Hobson T D C, Hutter O S, Birkett M, Veal T D, Durose K. Growth and characterization of Sb_2S_3 single crystals for fundamental studies. In: Proceedings of 2018 IEEE 7th World Conference on Photovoltaic Energy Conversion (WCPEC) (A Joint Conference of 45th IEEE PVSC, 28th PVSEC & 34th EU PVSEC). Waikoloa: IEEE, 2018, 0818–0822
20. Moy J P. Large area X-ray detectors based on amorphous silicon technology. Thin Solid Films, 1999, 337(1–2): 213–221

21. Jung N, Alving P L, Busse F, Conrads N, Meulenbrugge H M, Ruetten W, Schiebel U, Weibrecht M, Wieczorek H. Dynamic X-ray imaging system based on an amorphous silicon thin-film array. Physics of Medical Imaging, 1998, 3336: 396–407
22. Zhao W, Law J, Waechter D, Huang Z, Rowlands J A. Digital radiology using active matrix readout of amorphous selenium: detectors with high voltage protection. Medical Physics, 1998, 25 (4): 539–549
23. Zhao W, Rowlands J A. Digital radiology using active matrix readout of amorphous selenium: theoretical analysis of detective quantum efficiency. Medical Physics, 1997, 24(12): 1819–1833
24. Kasap S, Frey J B, Belev G, Tousignant O, Mani H, Laperriere L, Reznik A, Rowlands J A. Amorphous selenium and its alloys from early xeroradiography to high resolution X-ray image detectors and ultrasensitive imaging tubes. Physica Status Solidi (B), 2009, 246 (8): 1794–1805
25. XCOM. Photon Cross Sections Database: NIST Standard Reference Database 8 (NIST, 2013). Available at physics.nist.gov/PhysRefData/Xcom/html/xcom1.html
26. Yakunin S, Dirin D N, Shynkarenko Y, Morad V, Cherniukh I, Nazarenko O, Kreil D, Nauser T, Kovalenko M V. Detection of gamma photons using solution-grown single crystals of hybrid lead halide perovskites. Nature Photonics, 2016, 10(9): 585–589
27. Wei H, Fang Y, Mulligan P, Chuirazzi W, Fang H H, Wang C, Ecker B R, Gao Y, Loi M A, Cao L, Huang J. Sensitive X-ray detectors made of methylammonium lead tribromide perovskite single crystals. Nature Photonics, 2016, 10(5): 333–339
28. Ji C M, Wang S S, Wang Y X, Chen H X, Li L N, Sun Z H, Sui Y, Wang S A, Luo J H. 2D hybrid perovskite ferroelectric enables highly sensitive X-ray detection with low driving voltage. Advanced Functional Materials, 2020, 30(5): 1905529
29. Zhou Y, Wang L, Chen S, Qin S, Liu X, Chen J, Xue D, Luo M, Cao Y, Cheng Y, Sargent E H, Tang J. Thin-film Sb_2Se_3 photovoltaics with oriented one-dimensional ribbons and benign grain boundaries. Nature Photonics, 2015, 9(6): 409–415
30. Chen C, Bobela D C, Yang Y, Lu S, Zeng K, Ge C, Yang B, Gao L, Zhao Y, Beard M C, Tang J. Characterization of basic physical properties of Sb_2Se_3 and its relevance for photovoltaics. Frontiers of Optoelectronics, 2017, 10(1): 18–30
31. Zhao M, Su J, Zhao Y, Luo P, Wang F, Han W, Li Y, Zu X, Qiao L, Zhai T. Sodium-mediated epitaxial growth of 2D ultrathin Sb_2Se_3 flakes for broadband photodetection. Advanced Functional Materials, 2020, 30(13): 1909849
32. Kondrotas R, Zhang J, Wang C, Tang J. Growth mechanism of Sb_2Se_3 thin films for photovoltaic application by vapor transport deposition. Solar Energy Materials and Solar Cells, 2019, 199: 16–23
33. Li Z, Liang X, Li G, Liu H, Zhang H, Guo J, Chen J, Shen K, San X, Yu W, Schropp R E I, Mai Y. 9.2%-efficient core-shell structured antimony selenide nanorod array solar cells. Nature Communications, 2019, 10(1): 125
34. Yuan C, Jin X, Jiang G, Liu W, Zhu C. Sb_2Se_3 solar cells prepared with selenized dc-sputtered metallic precursors. Journal of Materials Science Materials in Electronics, 2016, 27(9): 8906–8910
35. Phillips L J, Savory C N, Hutter O S, Yates P J, Shiel H, Mariotti S, Bowen L, Birkett M, Durose K, Scanlon D O, Major J D. Current enhancement via a TiO_2 window layer for CSS Sb_2Se_3 solar cells: Performance limits and high V_{OC}. IEEE Journal of Photovoltaics, 2019, 9(2): 544–551
36. Wen X, Chen C, Lu S, Li K, Kondrotas R, Zhao Y, Chen W, Gao L, Wang C, Zhang J, Niu G, Tang J. Vapor transport deposition of antimony selenide thin film solar cells with 7.6% efficiency. Nature Communications, 2018, 9(1): 2179
37. Tang R, Zheng Z H, Su Z H, Li X J, Wei Y D, Zhang X H, Fu Y Q, Luo J T, Fan P, Liang G X. Highly efficient and stable planar heterojunction solar cell based on sputtered and post-selenized Sb_2Se_3 thin film. Nano Energy, 2019, 64: 103929
38. Li K, Chen C, Lu S, Wang C, Wang S, Lu Y, Tang J. Orientation engineering in low-dimensional crystal-structural materials via seed screening Sb_2Se_3. Advanced Materials, 2019, 31(44): 1903914
39. Kasap S O. X-ray sensitivity of photoconductors: application to stabilized a-Se. Journal of Physics D, Applied Physics, 2000, 33 (21): 2853–2865
40. Cousins P J, Neuhaus D H, Cotter J E. Experimental verification of the effect of depletion-region modulation on photoconductance lifetime measurements. Journal of Applied Physics, 2004, 95(4): 1854–1858
41. Li K, Kondrotas R, Chen C, Lu S, Wen X, Li D, Luo J, Zhao Y, Tang J. Improved efficiency by insertion of $Zn_{1-x}Mg_xO$ through sol-gel method in ZnO/Sb_2Se_3 solar cell. Solar Energy, 2018, 167: 10–17
42. Wang C, Lu S, Li S, Wang S, Lin X, Zhang J, Kondrotas R, Li K, Chen C, Tang J. Efficiency improvement of flexible Sb_2Se_3 solar cells with non-toxic buffer layer via interface engineering. Nano Energy, 2020, 71: 104577
43. Pan W, Yang B, Niu G, Xue K H, Du X, Yin L, Zhang M, Wu H, Miao X S, Tang J. Hot-pressed $CsPbBr_3$ quasi-monocrystalline film for sensitive direct X-ray detection. Advanced Materials, 2019, 31 (44): 1904405
44. Tokuda S, Adachi S, Sato T, Yoshimuta T, Nagata H, Uehara K, Izumi Y, Teranuma O, Yamada S. Experimental evaluation of a novel CdZnTe flat-panel X-ray detector for digital radiography and fluoroscopy. In: Proceedings of SPIE 4320, Medical Imaging 2001: Physics of Medical Imaging. San Diego: SPIE, 2001, 4320: 140–147
45. Basiricò L, Ciavatti A, Cramer T, Cosseddu P, Bonfiglio A, Fraboni B. Direct X-ray photoconversion in flexible organic thin film devices operated below 1 V. Nature Communications, 2016, 7(1): 13063
46. Temiño I, Basiricò L, Fratelli I, Tamayo A, Ciavatti A, Mas-Torrent M, Fraboni B. Morphology and mobility as tools to control and unprecedentedly enhance X-ray sensitivity in organic thin-films. Nature Communications, 2020, 11(1): 2136
47. Liang H L, Cui S J, Su R, Guan P F, He Y H, Yang L H, Chen L M, Zhang Y H, Mei Z X, Du X L. Flexible X-ray detectors based on amorphous Ga_2O_3 thin films. ACS Photonics, 2019, 6(2): 351–359
48. Yakunin S, Sytnyk M, Kriegner D, Shrestha S, Richter M, Matt G J, Azimi H, Brabec C J, Stangl J, Kovalenko M V, Heiss W. Detection of X-ray photons by solution-processed lead halide perovskite. Nature Photonics, 2015, 9(7): 444–449
49. Tsai H, Liu F, Shrestha S, Fernando K, Tretiak S, Scott B, Vo D T, Strzalka J, Nie W. A sensitive and robust thin-film X-ray detector

using 2D layered perovskite diodes. Science Advances, 2020, 6(15): eaay0815

50. Basiricò L, Senanayak S P, Ciavatti A, Abdi-Jalebi MFraboni BSirringhaus H. Detection of X-rays by solution-processed cesium-containing mixed triple cation perovskite thin films. Advanced Functional Materials, 2019, 29(34): 1902346
51. Mescher H, Schackmar F, Eggers H, Abzieher T, Zuber M, Hamann E, Baumbach T, Richards B S, Hernandez-Sosa G, Paetzold U W, Lemmer U. Flexible inkjet-printed triple cation perovskite X-ray detectors. ACS Applied Materials & Interfaces, 2020, 12(13): 15774–15784
52. Budil K S, Perry T S, Bell P M, Hares J D, Miller P L, Peyser T A, Wallace R, Louis H, Smith D E. The flexible X-ray imager. Review of Scientific Instruments, 1996, 67(2): 485–488
53. Kuo T T, Wu C M, Lu H H, Chan I, Wang K, Leou K C. Flexible X-ray imaging detector based on direct conversion in amorphous selenium. Journal of Vacuum Science & Technology A, Vacuum, Surfaces, and Films, 2014, 32(4): 041507
54. Sun H, Zhao B, Yang D, Wangyang P, Gao X, Zhu X. Flexible X-ray detector based on sliced lead iodide crystal. Phyica Status Solidi (RRL)-Rapid Research Letters, 2017, 11(2): 1600397

Chong Wang is a Ph.D. candidate at Wuhan National Laboratory for Optoelectronics, Huazhong University of Science and Technology, China, with a major in optical engineering. He received his Bachelor's degree from Huazhong University of Science and Technology, China in 2015. His current research interest is novel semiconductor optoelectronic materials and devices.

Xinyuan Du received his Bachelor's degree from Huazhong University of Science and Technology, China in 2018. He is currently pursuing a Ph.D. in optical engineering. He focuses on perovskite X-ray detection.

Siyu Wang is pursuing a master's degree at Wuhan National Laboratory for Optoelectronics, Huazhong University of Science and Technology, China. She works on the material properties of antimony selenide and its optoelectronic devices.

Hui Deng received his Ph.D. degree from Huazhong University of Science and Technology, China in 2019. He worked as an assistant professor at Fuzhou University, China after graduation. He has extensive experience in thin-film materials, solar cells, and photodetectors. He has published over 30 science citation index (SCI) journal papers, and his current SCI H-index is 18.

Chao Chen received his B.Sc. degree from School of Physics, Huazhong University of Science and Technology, China in 2014. From 2014/09 to 2019/02, he studied at Wuhan National Laboratory for Optoelectronics, Huazhong University of Science and Technology, China as a doctoral candidate and received his Ph.D. degree in 2019/02. Currently, he is a postdoctoral fellow at Wuhan National Laboratory for Optoelectronics, Huazhong University of Science and Technology, China. His research interests are thin-film solar cells and photodetectors.

Guangda Niu is an associate professor at Wuhan National Laboratory for Optoelectronics, Huazhong University of Science and Technology, China. He obtained his Ph.D. degree from Tsinghua University, China in 2016. His research interest is solar cells and photodetectors based on perovskite single crystal, thin films, and quantum dots.

Jincong Pang received his Bachelor's degree from Huazhong University of Science and Technology, China in 2019, and he is currently pursuing a Ph.D. in optical engineering. He focuses on single crystal X-ray detectors.

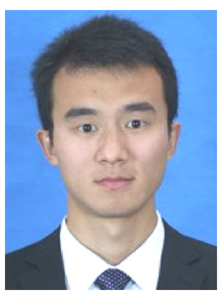

Kanghua Li received his Bachelor's degree from Huazhong University of Science and Technology, China in 2015. Subsequently, he joined Wuhan National Laboratory for Optoelectronics, Huazhong University of Science and Technology, China as a Ph.D. candidate. He mainly works on new inorganic photovoltaic materials and thin-film solar cells.

Shuaicheng Lu obtained his Bachelor's degree from Huazhong University of Science and Technology, China in 2016. Thereafter, he joined Wuhan National Laboratory for Optoelectronics, Huazhong University of Science and Technology, China as a Ph.D. candidate. His research interests include quasi-one-dimensional photovoltaic semiconductors and physical characterization techniques for photovoltaic materials and devices.

Xuetian Lin is a master's student at Huazhong University of Science and Technology, China and Paris Sciences & Lettres (PSL) Research University, France. She majors in new energy science and technology at China–EU Institute for Clean and Renewable Energy, Huazhong University of Science and Technology, China. She also majored in clean and renewable energy at PSL Research University, France. She mainly works on photovoltaic materials.

Haisheng Song received his Ph.D. degree from City University of Hong Kong, China, under the supervision of Prof. Wenjun Zhang in 2010. Thereafter, he moved to Japan and finished his postdoctoral research at National Institute for Material Science, Japan. After that, he joined Huazhong University of Science and Technology, China as an associate professor in 2012 and was promoted to full professor in 2018. His research interests include full-inorganic new conception thin-film photovoltaics, particularly the supplementary PVs for commercial Si technology, X-ray detection materials, and short-wave infrared detectors in CMOS compatible focal panel arrays.

Jiang Tang is a professor at Wuhan National Laboratory for Optoelectronics, Huazhong University of Science and Technology, China. He obtained his Ph.D. degree from University of Toronto, Canada in 2010. His research interest is optoelectronic devices, including X-ray and infrared detectors, thin-film solar cells, and light-emitting diodes. He has published over 150 papers, filed over 30 patents, and received the funding from the National Natural Science Foundation of China.

Supporting Information

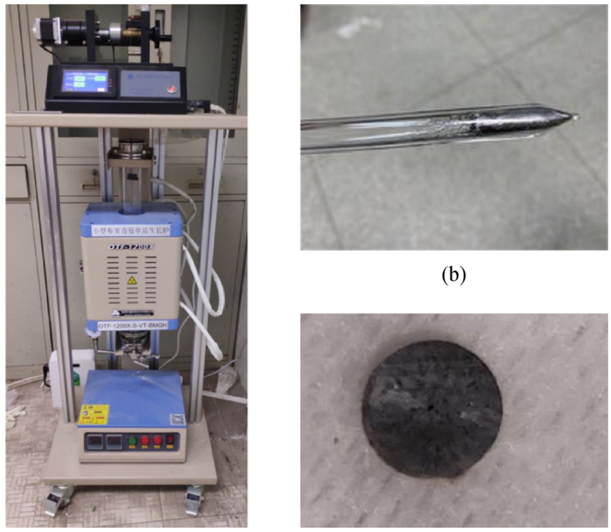

(a) (b) (c)

Fig. S1 (a) Photo of the vertical Bridgman furnace. (b) Photo of the obtained Sb_2Se_3 single crystal as prepared in a quartz ampoule. (c) Photo of the Sb_2Se_3 single crystal slice

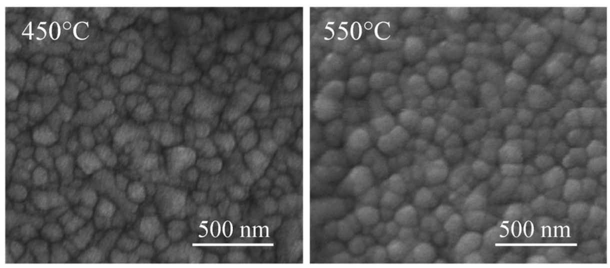

(a) (b)

Fig. S2 (a) SEM image of the TiO_2 layer annealed at 450°C with many small TiO_2 grains and high roughness. (b) SEM image of the TiO_2 layer annealed at 550°C with a relatively smooth grain surface

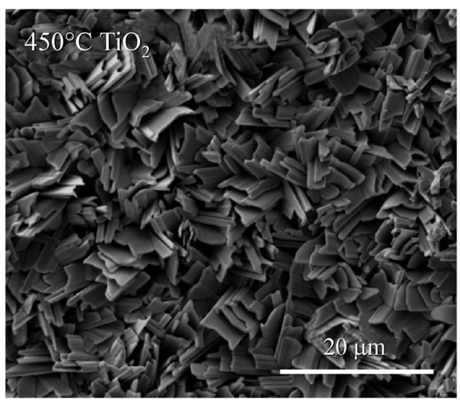

Fig. S3 SEM image of the Sb_2Se_3 film deposited on a TiO_2 substrate annealed at 450°C (substrate temperature: 400°C, source temperature: 600°C)

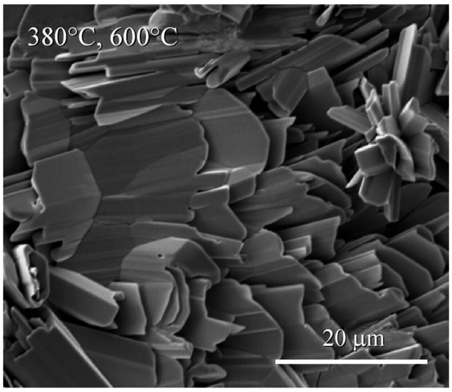

Fig. S4 SEM image of the Sb_2Se_3 film deposited at a relatively low substrate temperature of 380°C (source temperature: 600°C; the TiO_2 substrate was annealed at 550°C)

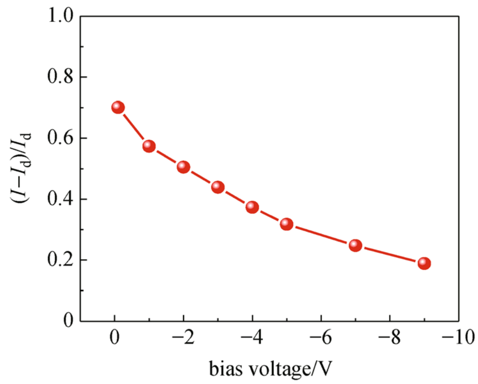

Fig. S5 Photocurrent amplitude (DI/I) as a function of the applied bias

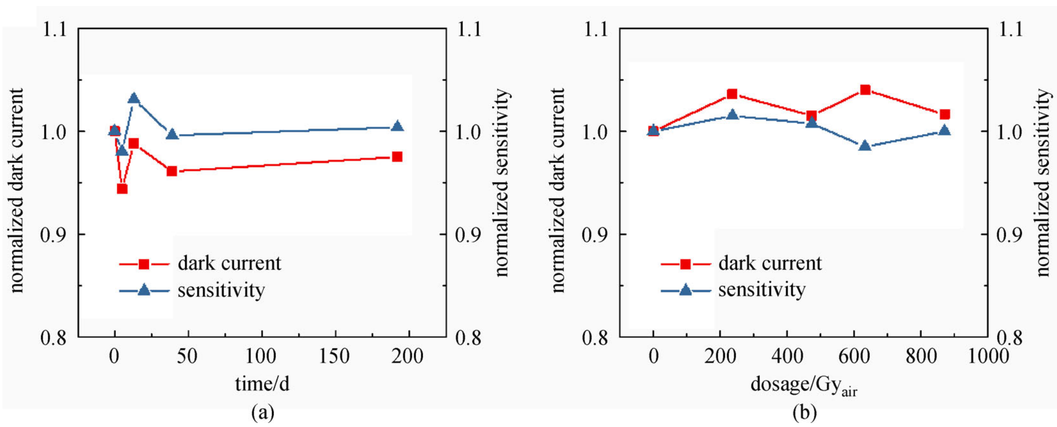

Fig. S6 (a) Stability performance of TiO_2/Sb_2Se_3 devices in air. (b) Radiation hardness performance of TiO_2/Sb_2Se_3 devices